

Plasma models for real-time control of advanced tokamak scenarios

D. Moreau¹, D. Mazon¹, M.L. Walker², J.R. Ferron²,
K.H. Burrell², S.M. Flanagan², P. Gohil², R.J. Groebner²,
A.W. Hyatt², R.J. La Haye², J. Lohr², F. Turco², E. Schuster³,
Y. Ou³, C. Xu³, Y. Takase⁴, Y. Sakamoto⁵, S. Ide⁵, T. Suzuki⁵ and
ITPA-IOS group members and experts

¹ CEA, IRFM, 13108 Saint-Paul-lez-Durance, France

² General Atomics, San Diego, CA 92186, USA

³ Department of Mechanical Engineering and Mechanics, Lehigh University, Bethlehem, PA 18015, USA

⁴ Graduate School of Frontier Sciences, The University of Tokyo, 277-8561, Kashiwa, Japan

⁵ Japan Atomic Energy Agency, Naka, Ibaraki 311-0193, Japan

E-mail: didier.moreau@cea.fr

Received 21 December 2010, accepted for publication 29 March 2011

Published 10 May 2011

Online at stacks.iop.org/NF/51/063009

Abstract

An integrated plasma profile control strategy, *ARTAEMIS*, is being developed for extrapolating present-day advanced tokamak (AT) scenarios to steady-state operation. The approach is based on semi-empirical modelling and was initially explored on JET (Moreau *et al* 2008 *Nucl. Fusion* **48** 106001). This paper deals with the general applicability of this strategy for simultaneous magnetic and kinetic control on various tokamaks. The determination of the *device-specific, control-oriented models* that are needed to compute optimal controller matrices for a given operation scenario is discussed. The methodology is generic and can be applied to any device, with different sets of heating and current drive actuators, controlled variables and profiles. The system identification algorithms take advantage of the large ratio between the magnetic and thermal diffusion time scales and have been recently applied to both JT-60U and DIII-D data. On JT-60U, an existing series of high bootstrap current ($\sim 70\%$), 0.9 MA non-inductive AT discharges was used. The actuators consisted of four groups of neutral beam injectors aimed at perpendicular injection (on-axis and off-axis), and co-current tangential injection (also on-axis and off-axis). On DIII-D, dedicated system identification experiments were carried out in the loop voltage (V_{ext}) control mode (as opposed to current control) to avoid feedback in the response data from the primary circuit. The reference plasma state was that of a 0.9 MA AT scenario which had been optimized to combine non-inductive current fractions near unity with $3.5 < \beta_N < 3.9$, bootstrap current fractions larger than 65% and $H_{98(y,2)} = 1.5$. Actuators other than V_{ext} were co-current, counter-current and balanced neutral beam injection, and electron cyclotron current drive. Power and loop voltage modulations resulted in dynamic variations of the plasma current between 0.7 and 1.2 MA. It is concluded that the response of essential plasma parameter profiles to specific actuators of a given device can be satisfactorily identified from a small set of experiments. This provides, for control purposes, a *readily available* alternative to first-principles plasma modelling.

(Some figures in this article are in colour only in the electronic version)

1. Introduction

The design of an economically attractive steady-state fusion reactor relies on the development of so-called advanced tokamak (AT) operation scenarios in which an optimization of some plasma parameter profiles results in a large improvement in fusion performance, at reduced plasma current [1–3]. A high-gain fusion burn could then be achieved while a major fraction of the toroidal current is self-generated by the neo-classical bootstrap effect. However, in present-day

experiments, the high performance phase is often limited in duration by transport and MHD phenomena. Advanced plasma control and in particular real-time control of the magneto-thermal plasma state generally referred to as *magneto-kinetic control* (or simply *kinetic control*) are therefore of paramount importance for the extrapolation of the scenarios to steady-state operation in ITER [4, 5] and for the development of nuclear fusion as an attractive source of energy.

In a tokamak, the multiple magnetic and fluid or kinetic parameter profiles which define the plasma state (poloidal

magnetic flux, safety factor, plasma density, velocity, pressure, etc) are known to be strongly coupled, and the heating and current drive (H&CD) control actuators are generally quite constrained and limited in number. Among the most commonly used H&CD systems are neutral beam injection (NBI), electron cyclotron resonance heating (ECRH) or current drive (ECCD), ion cyclotron resonance heating (ICRH), fast wave current drive (FWCD) and lower hybrid current drive (LHCD). Although non-linear, the linkage between the various plasma parameters can be taken as an advantage for controller design because the effective number of controlled profiles can be reduced to a small set of essential ones. There is no general method, however, to take into account non-linearities in the design of controllers and, for tokamak kinetic control, accurate non-linear plasma models are not available yet. But, in many cases, controllers based on empirically identified linear response models [6] provide satisfactory results. If the system is linearized around an equilibrium which is close enough to the target, linear control will be effective in regulating the system at the target, even in the presence of various disturbances. Multiple-input–multiple-output (MIMO) control of the safety factor profile based on the *static* linear response to three H&CD actuators has been reported on JET [7]. The same model-based technique was then applied, with partial success, to the simultaneous control of the safety factor profile and of a kinetic parameter profile, the electron temperature gradient [8], but clear limitations came from the use of the static response model to describe a system in which the magneto-kinetic dynamics is important, and takes place on two, significantly different, time scales.

If, however, an approximate two-time-scale linear response model can be empirically identified for the most relevant magnetic and kinetic parameter profiles subject to specific actuators, *while retaining essential couplings between all parameters*, then an integrated feedback controller can be designed to regulate the *global plasma state* through a minimization algorithm [7–9]. For any chosen set of target profiles, the *closest self-consistent plasma state achievable with the available actuators* can be defined with an appropriate metric, and it will then be reached and sustained by the regulatory action of feedback control, provided that the approximate response model is relatively accurate for the given operation scenario, in some broad vicinity of the target state. With a small number of actuators, this global state control represents a reasonable objective to pursue rather than attempting to control each plasma parameter or profile accurately and independently with a specific actuator. Based on this philosophy, proof-of-principle profile control experiments were performed in 2007 on JET. The results were published in [9], together with a complete description of the system identification scheme, underlying assumptions and justifications, mathematical developments and control algorithms for the general case of magneto-fluid plasma state control. This can include, for example, the simultaneous control of the current density, plasma rotation, ion and electron temperature and/or pressure profiles. Then, in order to demonstrate that the method has a large potential and is generic in that it can be applied to any tokamak and any set of actuators, joint experiments have been proposed on other large fusion devices with AT operation capability. These experiments have

been carried out under the framework of the International Tokamak Physics Activity for Integrated Operation Scenarios (ITPA-IOS).

This paper focuses on the identification of *control-oriented magneto-fluid plasma models* from experimental data obtained on JT-60U and DIII-D. The semi-empirical, physics-based ARTAEMIS⁶ approach referred to above, and followed here, is motivated by the fact that a real-time magneto-kinetic control strategy based on first-principles (e.g. gyrokinetic) plasma models is as yet unaffordable. This is partly because turbulent transport models are not mature enough to make real-time predictions of the detailed dynamic response of the plasma profiles, but also because they are extremely complex and not really suited for real-time applications. Indeed, the approach developed here provides, for control purposes, a pragmatic and *readily available* alternative to first-principles plasma modelling. By showing that the dynamics of the magneto-fluid parameter profiles can be satisfactorily modelled on various tokamaks by the same semi-empirical technique, this paper provides a validation of the system identification methodology, and therefore offers the perspective of successful plasma control applications.

The state-space structure [6] of the models to be experimentally identified has been naturally obtained from a simplified set of transport equations which are projected on appropriate radial basis functions through a Galerkin scheme [9]. The model order is then further reduced using the theory of singularly perturbed systems in which the small parameter, ε , represents the typical ratio of the thermal and resistive diffusion time scales. The state-space formalism is therefore particularly suited to the problem, because it allows singular perturbation methods to be used. A near-optimal control algorithm can therefore be rigorously developed within the two-time-scale approximation, yielding the optimal control law correct to order ε^2 [10]. Thus, starting from a set of appropriate data, the ARTAEMIS algorithms generate two coupled dynamic models, a slow model that evolves the various parameters on the resistive time scale and a fast one for the evolution of the system on the particle, momentum and thermal diffusion time scale. They also generate the various gain matrices that should be loaded into the corresponding near-optimal two-time-scale controller.

The next section describes the choice of the relevant state variables, and the structure of the reduced state-space models based on a general analysis of the plasma transport equations. Then, in section 3, the proposed system identification method is applied to existing JT-60U data. A model for the coupled response of the safety factor and of the toroidal rotation profiles to four neutral beam actuators is obtained. In section 4, dedicated modulation experiments performed on DIII-D are described, and the results of the model identification for the coupled dynamics of the poloidal magnetic flux and toroidal rotation profiles are reported. Finally some conclusions will be drawn.

⁶ The two-time-scale system identification and plasma state control algorithms described in [9] and based on applying the theory of singularly perturbed systems to a set of simplified plasma transport equations will hereafter be referred to using the acronym ARTAEMIS (for ‘advanced real-time algorithms based on empirical modelling of integrated scenarios’).

2. Two-time-scale state-space structure of the ARTAEMIS plasma models

When the usual set of plasma transport equations are averaged over magnetic flux surfaces they yield a one-dimensional model in which all physical variables depend only on a radial variable, x , and on time. The system is linearized around an equilibrium state which is referred to as the *reference state*, and *which need not be known explicitly*. A state-space model of minimal complexity is then found, within assumptions that have been made to keep the system order within reasonable limits and its experimental identification tractable [9]. The state variables appear naturally to be the variations of the internal poloidal magnetic flux, Ψ , and of a set of fluid/kinetic variables such as the plasma density, n , toroidal velocity, V_ϕ , and temperature, T (ideally $[T_i, T_e]$), with respect to their reference values. One can then introduce some unknown linear differential operators, $\mathcal{L}_{\alpha,\beta}\{x\}$, and row vectors, $L_{\alpha,\beta}(x)$, depending upon the variable x but independent of time, such that the system under consideration reads

$$\frac{\partial \Psi(x, t)}{\partial t} = \mathcal{L}_{\Psi,\Psi}\{x\} \circ \Psi(x, t) + \mathcal{L}_{\Psi,K}\{x\} \circ \begin{bmatrix} n(x, t) \\ V_\phi(x, t) \\ T(x, t) \end{bmatrix} + L_{\Psi,P}(x) \cdot P(t) + V_{\text{ext}}(t) \quad (1a)$$

$$\varepsilon \frac{\partial}{\partial t} \begin{bmatrix} n(x, t) \\ V_\phi(x, t) \\ T(x, t) \end{bmatrix} = \mathcal{L}_{K,\Psi}\{x\} \circ \Psi(x, t) + \mathcal{L}_{K,K}\{x\} \circ \begin{bmatrix} n(x, t) \\ V_\phi(x, t) \\ T(x, t) \end{bmatrix} + L_{K,P}(x) \cdot P(t) \quad (1b)$$

with inputs $P(t) = [P_1(t), P_2(t), P_3(t), \text{etc}]$, the heating, fuelling and current drive inputs, e.g. powers from NBI, ICRH, ECCD, LHCD, FWCD, gas injection, etc, and V_{ext} , the plasma surface loop voltage. Here, the \circ symbol means that the operator, $\mathcal{L}_{\alpha,\beta}\{x\}$, which is on the left of the symbol, is to be applied to the function of x that appears on the right. Normal dots represent the usual matrix product. The small parameter, ε ($\varepsilon \ll 1$, constant), represents the typical ratio between the characteristic time for the evolution of the kinetic parameters (equation (1b)) and the resistive diffusion time which characterizes the evolution of magnetic parameters (equation (1a)). It is introduced here to scale the operators $\mathcal{L}_{\Psi,\Psi}\{x\}$ and $\mathcal{L}_{K,K}\{x\}$ so that their smallest eigenvalues have similar magnitudes, and it allows singular perturbation methods to be applied in order to simplify both model identification and controller design.

A pragmatic way to identify the various operators in equations (1a) and (1b) is to resort to a finite set of trial basis functions on which to project the distributed plasma parameters, and to find the best least-square fits of the discrete system to experimental data. Ideally, one would try to retain the differential nature of the original system using appropriate techniques, rather than projecting the system onto a finite set of basis functions. There are indeed situations in which a genuine system of partial differential equations (PDEs) is definitely required to design a satisfactory distributed-parameter controller (a low-order discrete model would be inappropriate if high order modes were unstable). However,

because of the high dimensionality of the physical state space, the numerical identification of a comprehensive distributed-parameter model (equations (1a) and (1b)) can be anticipated to be extremely difficult. Therefore, unless the need for such a model becomes really apparent (there is *a priori* no need for this), and bearing in mind that the system identification will have to be made from noisy experimental data until an accurate tokamak plasma simulator is available, a discretization seems unavoidable. What is needed, at this level, is only an interpolation scheme that allows the data to be projected on a fixed radial grid and the system to be discretized. The choice of the interpolation/discretization scheme is not essential here because the data can be interpolated offline. It is simply assumed that, by increasing the space-time resolution of the data and the number of radial points and basis functions, the identified lumped-parameter system would converge towards the PDE model that would best fit the data. Nonetheless, a sufficient number of radial points is required if the original distributed-parameter system is to be fairly well approximated. The number of parameters to be identified rapidly increases with the order of the system and the number of points on the radial grid. The identification problem then becomes increasingly ill-conditioned, yielding solutions that are unphysical and unstable to small changes in the data. It was found that eight to ten equally spaced radii was a good compromise.

A Galerkin approach has been chosen for the interpolation of the data and the discretization of the system [9]. The projection of a generic dynamical variable, $Y(x, t)$, on the chosen basis functions then reads

$$Y(x, t) = \sum_{i=1}^N G_{y,i}(t) a_i(x) + R_{y,i}(x, t) \quad (2)$$

where $a_i(x)$ are the basis functions (e.g. cubic splines⁷) with $i = 1, 2, \dots, N$, and $R_{y,i}(x, t)$, are residues chosen to be orthogonal to every basis function:

$$\int_0^1 a_i(x) R_{y,i}(x, t) dx = 0. \quad (3)$$

The expansion coefficients, $G_{y,i}(t)$, will be called Galerkin coefficients and the vector array containing the Galerkin coefficients of the variable $Y(x, t)$ will simply be named $Y(t)$. After this discretization has been made, a lumped-parameter version of the state-space model is obtained, which reads

$$\dot{\Psi}(t) = A_{1,1} \cdot \Psi(t) + A_{1,2} \cdot \begin{bmatrix} n(t) \\ V_\phi(t) \\ T(t) \end{bmatrix} + B_1 \cdot P(t) + B_{\Psi,V} \cdot V_{\text{ext}}(t) \quad (4a)$$

$$\varepsilon \begin{bmatrix} \dot{n}(t) \\ \dot{V}_\phi(t) \\ \dot{T}(t) \end{bmatrix} = A_{2,1} \cdot \Psi(t) + A_{2,2} \cdot \begin{bmatrix} n(t) \\ V_\phi(t) \\ T(t) \end{bmatrix} + B_2 \cdot P(t) \quad (4b)$$

where parameter profiles are now represented by vectors, and where A_{hk} , B_h (with $h = 1, 2$ and $k = 1, 2$) are unknown matrices and $B_{\Psi,V}$ is a known matrix.

⁷ The set of basis functions could be different for each dynamical variable and must be chosen judiciously to provide satisfactory fits of the corresponding parameter profiles.

Part of the difficulty in identifying the various matrices in equations (4a) and (4b) stems from the fact that widely varying time scales are involved in the dynamics of the system. Indeed, the order of magnitude of the parameter, ε , introduced above is about 0.05 in present tokamaks, and it will be even smaller in burning plasmas, as in ITER. It therefore seems judicious to take advantage of this ordering parameter and to use identification and control techniques which are based upon the theory of singularly perturbed systems and multiple-time-scale expansions [10]. This amounts to expanding each dependent variable in powers of ε , defining an additional independent variable, $\tau = t/\varepsilon$, to describe the fast dynamics while t describes the slow dynamics, and to splitting variables into a sum of a fast and a slow component which depend on τ and t , respectively. A well-posed set of ordinary differential equations is then obtained by grouping terms of equal order in ε and imposing the condition that, in the asymptotic limit where ε tends to zero, the initial conditions for the slow dynamics ($t = 0$) match the quasi-steady-state solution on the fast dynamics ($\tau \rightarrow \infty$).

It is clear from the structure of the original system that the magnetic variable, $\Psi(t)$, has only a slow evolution because there is no term of order $1/\varepsilon$ in the $d\Psi/dt$ expansion. Following [9, 10], we shall therefore seek two models of reduced orders, a slow model

$$\dot{\Psi}(t) = A_S \cdot \Psi(t) + B_S \cdot \begin{bmatrix} P_S(t) \\ V_{\text{ext},S}(t) \end{bmatrix}$$

$$\text{with } \begin{bmatrix} n_{S}(t) \\ V_{\Phi,S}(t) \\ T_S(t) \end{bmatrix} = C_S \cdot \Psi(t) + D_S \cdot P_S(t) \quad (5)$$

and a fast model:

$$\begin{bmatrix} \dot{n}_F(t) \\ \dot{V}_{\Phi,F}(t) \\ \dot{T}_F(t) \end{bmatrix} = A_F \cdot \begin{bmatrix} n_F(t) \\ V_{\Phi,F}(t) \\ T_F(t) \end{bmatrix} + B_F \cdot P_F(t) \quad (6)$$

where any input or fluid/kinetic variable, X , is to be split into a slow and a fast component, X_S and X_F , respectively, according to $X = X_S + X_F$. The slow linkage between the magnetic equilibrium and the fluid and kinetic parameter profiles is represented, in its linearized form, by the C_S matrix.

Now, although the poloidal magnetic flux appears as a natural state variable, one may sometimes find it more practical, depending on the application, to perform magnetic control through the inverse safety factor profile, $\iota(x)$, a non-dimensional parameter that is defined by $\iota(x) = 1/q(x) = d\Psi(x)/d\Phi(x)$ where $\Phi(x)$ is the toroidal magnetic flux. At constant vacuum toroidal field and plasma shape, and when the radial variable, x , is defined as $(\Phi/\Phi_{\text{max}})^{1/2}$ where Φ_{max} is the toroidal flux within the last closed flux surface, $\Phi(x)$ depends weakly on the power inputs in comparison with $\Psi(x)$. Thus, for control purposes, an alternative state-space model can be sought where the linearized variations of $\iota(x)$ around a given equilibrium are assumed to map onto those of $\Psi(x)$, so that $\iota(x)$ can be substituted to $\Psi(x)$ in equations (5), and assumed to be the magnetic state variable. This substitution was indeed made for magnetic profile control experiments on JET [9] and will be illustrated in section 3, while $\Psi(x)$ will be retained as the magnetic state variable in section 4.

3. System identification from existing JT-60U data

The first extended version of the *ARTAEMIS* identification algorithm that allows a two-time-scale *magneto-fluid model* to be identified has been developed using existing JT-60U data typical of steady-state AT operation [11]. A series of nearly non-inductive discharges with more than 70% bootstrap current fractions were analysed (pulses #45862, and #45903–45914) and an iterative identification procedure was set up. It allowed the matrices A_S , B_S , C_S , D_S , A_F and B_F to be chosen in such a way that the model structure described above (equations (5) and (6)) best fits the data, while satisfying some mathematical and physical constraints that reduce the dimensionality of the unknown parameter space.

The reference plasma state was characterized by a magnetic field of 3.7 T, a fully non-inductive plasma current of 0.9 MA, and a central plasma density of $3 \times 10^{19} \text{ m}^{-3}$. The selected actuators consisted of four groups of neutral beam injectors corresponding to (i) on-axis perpendicular injection, (ii) off-axis perpendicular injection, (iii) on-axis co-current tangential injection, (iv) off-axis co-current tangential injection.

The selected output profiles were the inverse safety factor, $\iota(x) = 1/q(x)$, toroidal rotation velocity, $V_\Phi(x)$, and ion temperature, $T_i(x)$. In order to take into account the coupling of these variables with the plasma density although $n(x, t)$ is not considered here as a controlled variable, the line-averaged density was included as an additional input to the system (i.e. included in the vector $P(t)$ in equations (4a), (4b)–(6)). The output data were then interpolated on a unique radial grid for each parameter profile through a cubic-splines Galerkin approximation, and on a unique temporal grid through linear interpolation. The radial grids were chosen in relation to the availability of the data for the discharges under study, i.e. $x = 0.5, 0.6, 0.7, 0.8$ and 0.9 for $\iota(x)$, and $x = 0.2, 0.3, 0.4, 0.5, 0.6, 0.7$ and 0.8 for $V_\Phi(x)$. Examples of radial profiles of the safety factor and toroidal rotation velocity are shown in figures 1(a) and (b) where the original data and the cubic-splines Galerkin fits with knots on the radial grids given above can be compared (the rotation data for $x > 0.8$ were discarded in this analysis because the controller was originally designed for $0.1 \leq x \leq 0.8$). Typical time-dependent data used for system identification can then be seen in figure 2. Figure 2(a) shows the time evolution of the safety factor at $x = 0.6$ in various pulses in which the actuator inputs varied, and figure 2(b) shows the evolution of the toroidal velocity at $x = 0.2, 0.3, \dots, 0.8$ in pulse #45903. The large change in plasma rotation between $t = 7$ s and 8 s is mainly due to the replacement of 2 MW of tangential injection by 2 MW of perpendicular injection, as can be seen in figures 3(a) and (b).

The system identification was performed starting at $t = 6$ s, i.e. during the current flat top of the discharges, and through a number of iterations in which the data were projected onto subspaces of varying dimensions, following the general methodology described in [9]. In particular, in each dataset an offset corresponding to the average of the data in the time window under consideration is subtracted from the data, so that the identification routines only handle datasets with zero average while searching for the best linear response model. At each step of the identification process for a given plasma

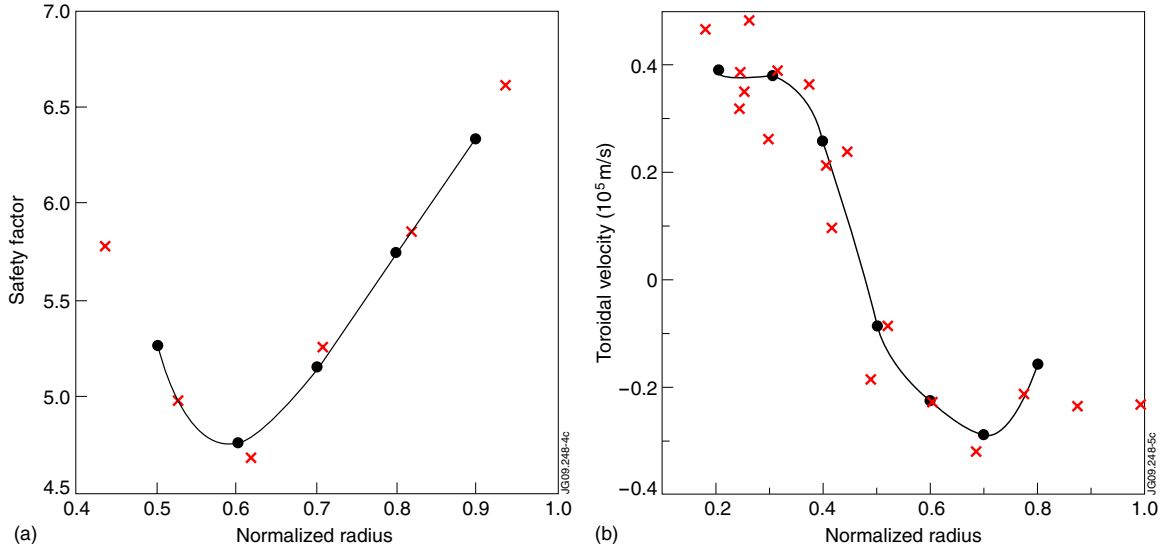


Figure 1. (a). Interpolation of the safety factor profile versus normalized radius on JT-60U (pulse #45903 at $t = 7$ s). The red crosses are experimental data and the black curve is the Galerkin fit using cubic-splines with knots shown by the black dots. (b) Interpolation of the toroidal velocity profile (10^5 m s $^{-1}$) versus normalized radius on JT-60U (pulse #45903 at $t = 7$ s). The red crosses are experimental data and the black curve is the Galerkin fit using cubic-splines with knots shown by the black dots (data at $x > 0.8$ are discarded).

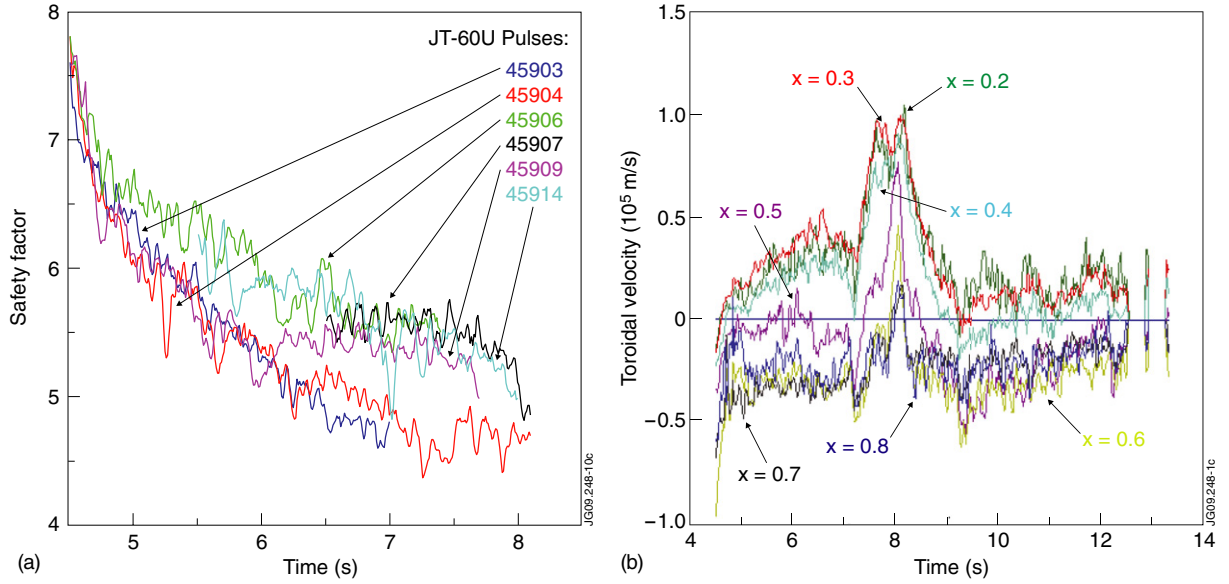


Figure 2. (a). Time evolution of the safety factor at $x = 0.6$ in JT-60U pulses #45903-04-06-07-09-14. (b) Time evolution of the toroidal velocity (10^5 m s $^{-1}$) at $x = 0.2, 0.3, 0.4, 0.5, 0.6, 0.7$ and 0.8 in JT-60U pulse #45903.

parameter profile, $Y(x, t)$, ARTAEMIS maximizes a global fit parameter, f , which is defined as

$$f = 1 - \left[\frac{\sum_{\text{samples}} \int_{x_1}^{x_2} (Y(x) - Y_{\text{sim}}(x))^2 dx}{\sum_{\text{samples}} \int_{x_1}^{x_2} (Y(x) - \langle Y(x) \rangle_{\text{samples}})^2 dx} \right]^{1/2} \quad (7)$$

where Y_{sim} represents the data simulated by the current model after reconstruction of the profiles from the basis functions and the Galerkin coefficients, $[x_1, x_2]$ is the radial window on which the model is to apply and $\langle Y(x) \rangle_{\text{samples}}$ stands for the average of the data over the time samples at a given radius.

The slow model was identified by considering the time evolution of five Galerkin coefficients of the $\iota(x, t)$ data at knots $x = 0.5, 0.6, 0.7, 0.8$ and 0.9 together with the input data, both filtered with a low-pass filter with a cutoff frequency of 4 Hz. The first iterations provided an approximation of the A_S matrix by selecting pulses with the least input variations, so that the slowest eigenmodes of the system can be better estimated. In subsequent iterations, the eigenmodes with the longest characteristic times were fixed when satisfactory fits could be obtained while searching for columns of the B_S matrix corresponding to different inputs. This was done gradually by selecting pulses where the respective inputs had been varied. After each satisfactory iteration, the static gain matrix of the model was updated and the new matrix was used to define the

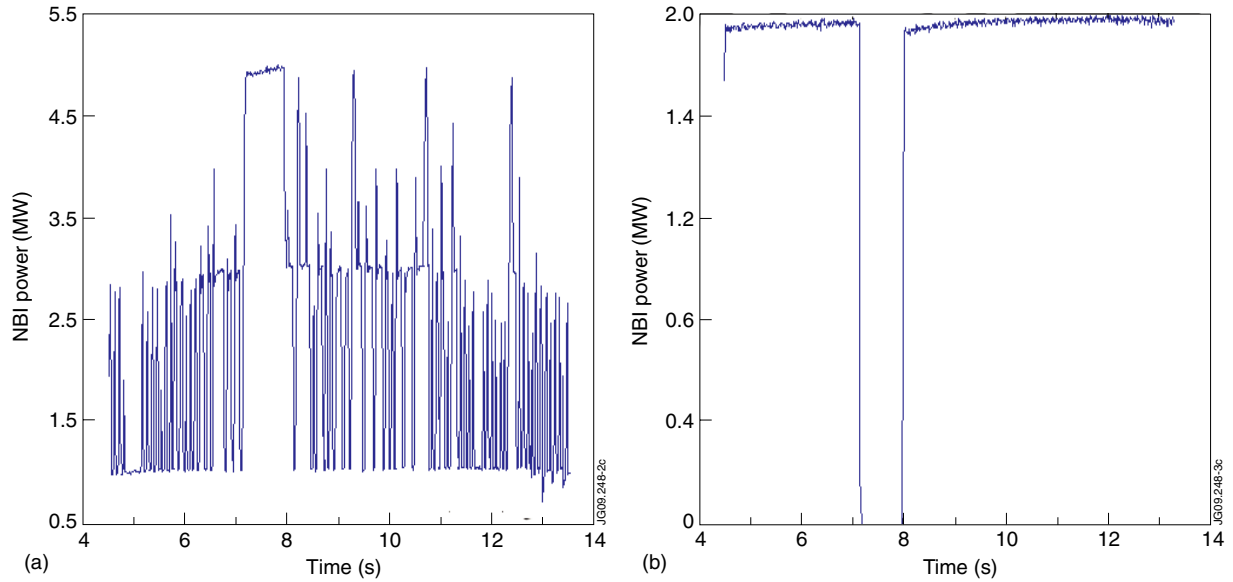


Figure 3. (a) Time evolution of the NBI power (MW) in JT-60U pulse #45903: perpendicular on-axis injection. (b) Time evolution of the NBI power (MW) in JT-60U pulse #45903: tangential on-axis injection.

subspace in which the following iterations were performed. The best model that was found for the evolution of $\iota(x, t)$ was finally a model of order four, while the dimension of the original data space was five since Galerkin coefficients were calculated at five radial knots. The four eigenvalues of the A_S matrix correspond to characteristic times of 3.28 s, 2.92 s, 1.23 s and 0.18 s.

The A_S and B_S matrices were then fixed when searching for the C_S , D_S matrices and for the fast model. There, the splitting between the slow and the fast components of the data to define the slow input vector, P_S , in equation (5) was made by filtering the data with a cutoff frequency of 1.25 Hz. This was the lowest frequency at which the inputs could be filtered while retaining a good fit of the unfiltered $\iota(x, t)$ data by the slow model. In order to show that the same method can be applied to various fluid/kinetic profiles, two models were identified, one for $V_\phi(x, t)$ coupled to $\iota(x, t)$ and one for $T_i(x, t)$ coupled to $\iota(x, t)$. Further couplings between $V_\phi(x, t)$ and $T_i(x, t)$ could be allowed to possibly improve the model if simultaneous control of these profiles was to be attempted. After removing the low frequency part of the data, below 1.25 Hz, the same iterative procedure was followed for determining the A_F and B_F matrices, as for the slow model.

For the identification of the matrices, C_S and D_S , that represent the slow coupling between the safety factor profile and both the toroidal rotation and ion temperature profiles, the $V_{\phi,F}$ and $T_{i,F}$ data predicted by the fast model using the high frequency part (above 1.25 Hz) of the inputs, P_F (equation (6)), were removed from the measurements before processing. The model for $V_\phi(x, t)$ was restricted to the radial knots $x = 0.4, 0.5, 0.6$ and 0.7 and the model for $T_i(x, t)$ to the radial knots from $x = 0.2$ to 0.7 (note that the $\iota(x, t)$ data were only available for $x \geq 0.5$). The best model that was found for the fast components of $V_\phi(x, t)$ was a model of order four whose characteristic times were 0.38 s, 0.15 s, 0.10 s and 0.015 s. For $T_i(x, t)$, the best model was of order six with characteristic times of 0.44 s, 0.20 s, 0.15 s, 0.13 s, 0.05 s and 0.04 s.

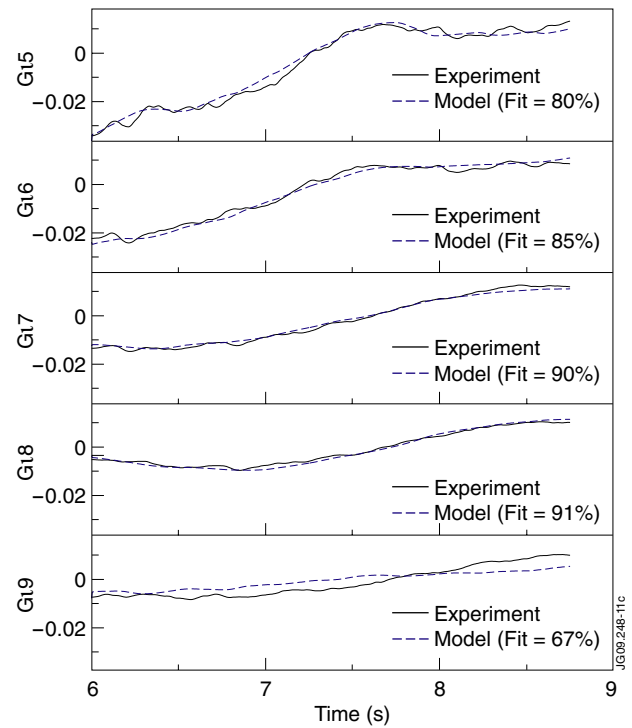


Figure 4. Comparison between the measured (black, full) and model-simulated (blue, dotted) $\iota = 1/q$ data versus time, at $x = 0.5, 0.6, 0.7, 0.8$ and 0.9 (JT-60U pulse #45862). Global fit: $f = 87\%$.

Figures 4–7 illustrate, for different plasma radii, typical comparisons between the zero-average measured data and the model simulations from which the same offset has been subtracted. An example of the slow model $\iota(x)$ response to the experimental actuator input data (equation (5)) is shown in figure 4 and can be compared with the experimental $\iota(x)$ response (the fast component of $\iota(x)$ that can be seen in figure 2(a) was attributed to noise, and disregarded). In

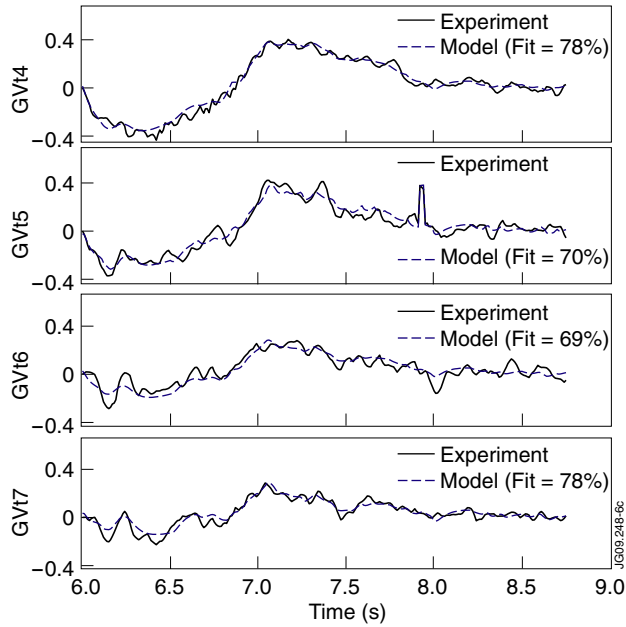


Figure 5. Comparison between the measured (black, full) and model-simulated (blue, dotted) V_ϕ data (10^5 m s^{-1}) versus time, at $x = 0.4, 0.5, 0.6$ and 0.7 (fast model, JT-60U pulse #45862). Global fit: $f = 73\%$.

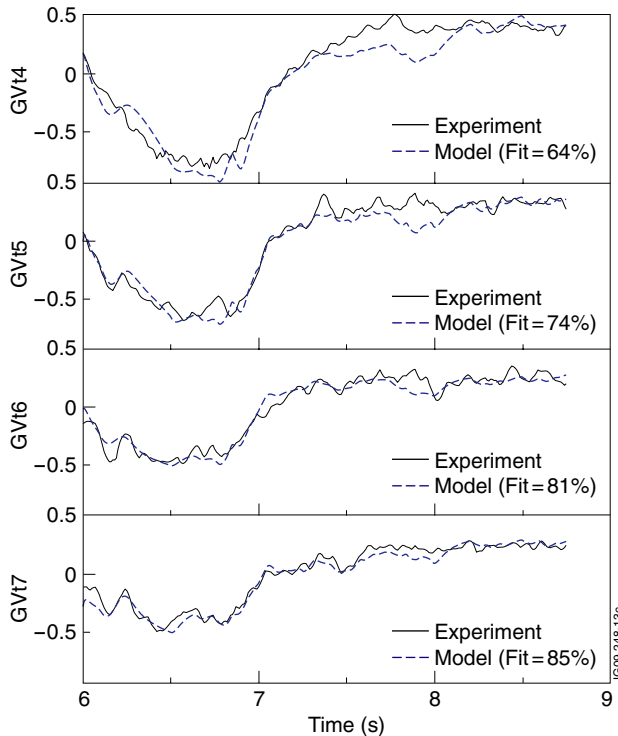


Figure 6. Comparison between the measured (black, full) and model-simulated (blue, dotted) V_ϕ data (10^5 m s^{-1}) at $x = 0.4, 0.5, 0.6$ and 0.7 (full model, JT-60U pulse #45862). Global fit: $f = 76\%$.

addition to the global fit parameter, f , defined in equation (7), local fit parameters have been defined using, in the numerator of formula (7), the error at a given radius weighted by $(x_2 - x_1)$ instead of its integral between x_1 and x_2 . They are displayed in each frame of the figures. The fast model $V_\phi(x)$ response to

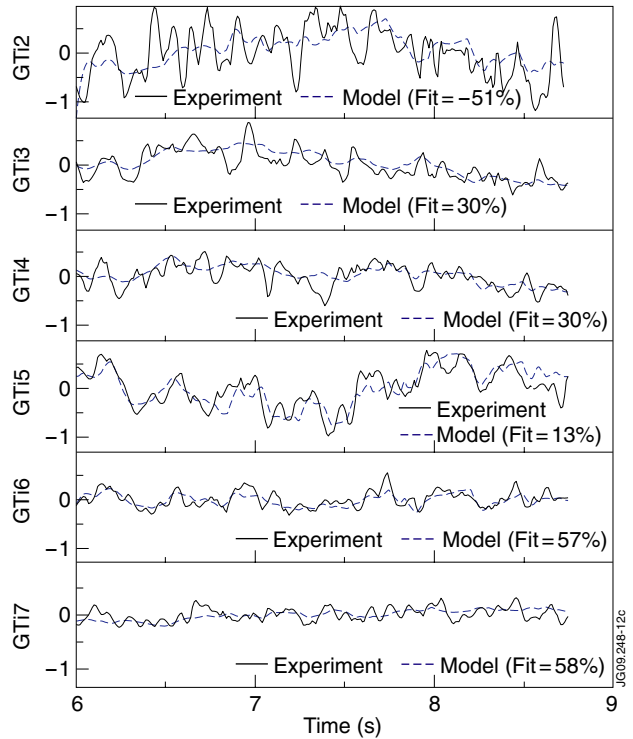


Figure 7. Comparison between the measured (black, full) and model-simulated (blue, dotted) T_i data (keV) at $x = 0.2, 0.3, 0.4, 0.5, 0.6$ and 0.7 (full model, JT-60U pulse #45862). Global fit: $f = 31\%$.

the fast component of the same actuator data (equation (6)) is shown in figure 5 and can be compared with the fast component of the experimental $V_\phi(x)$ response (the fit parameters are computed consistently, i.e. using only the fast component of the data). The responses from the full (two-time-scale) model combining the slow and fast models (equations (3), (4a) and (4b)) are shown for $V_\phi(x)$ and $T_i(x)$, and for the same discharge, in figures 6 and 7, respectively. It must be recalled that the JT-60U data used for system identification were gathered from a chosen set of pre-existing discharges and are not as rich as data obtained in dedicated modulation experiments (see next section). Therefore, here, the same data were used for the identification and the validation of the models.

Finally, to illustrate the potential use of the control-oriented models obtained above, we display in figures 8(a) and (b) the results of a typical closed-loop simulation based on a near-optimal two-time-scale controller whose design was thoroughly described in [9]. The simulation corresponds to a virtual discharge with the same field and current as pulse #45903, but with controller-driven NBI actuators. The inverse safety factor profile, $\iota(x)$, and the toroidal velocity profile, $V_\phi(x)$, are controlled using the four groups of NBI injectors, (i) to (iv), defined earlier and labelled Pnb1 to Pnb4, respectively, in figure 8(a). The line-integrated density is assumed constant here, but its variations could be feedforward compensated in real-time. In these linear simulations whose only purpose is to validate the controller design and the associated software, the inputs to the controller, i.e. the ‘measured data’ or the error signals between the ‘measured data’ and the target profiles, must of course be provided by an *ad hoc* plasma

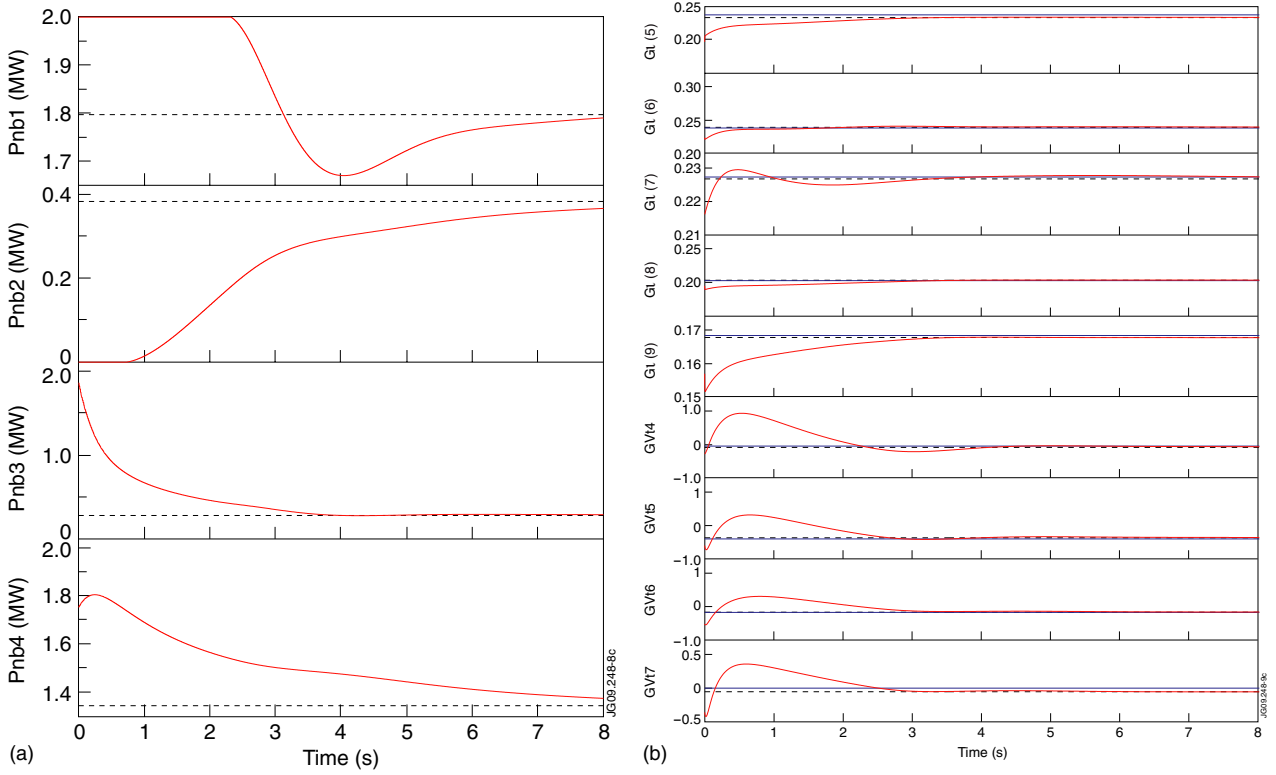


Figure 8. (a). Evolution of the actuator powers in the closed-loop simulation. The time origin refers to the start of the control phase. The dotted lines show the final values of the actuators, as expected from the steady-state gain of the closed-loop system. (b) Evolution of $\iota(x)$ at $x = 0.5-0.9$ (five upper traces) and $V_\phi(x)$ at $x = 0.4-0.7$ (four lower traces) in the closed-loop simulation. The requested target values are represented by the full horizontal lines. The dotted lines show the final values of the controlled parameters, as expected from the steady-state gains of the closed-loop system.

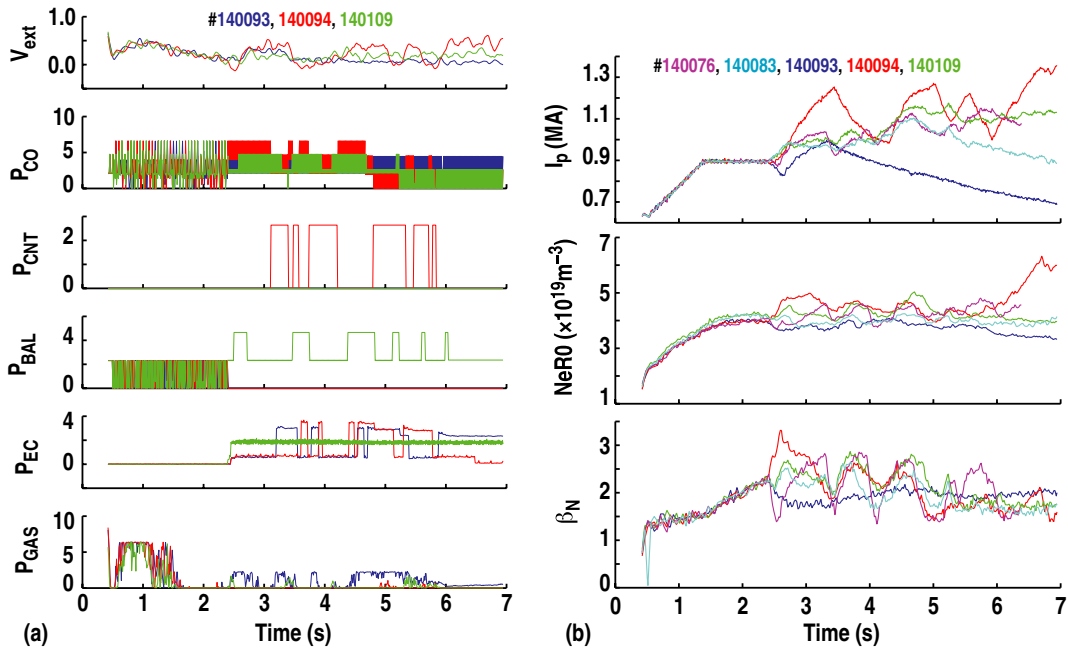


Figure 9. (a). Time evolution of V_{ext} , P_{CO} , P_{CNT} , P_{BAL} , P_{EC} and P_{GAS} in DIII-D shots #140093, 140094 and 140109. (b) Time evolution of I_p , line-averaged density and β_N in DIII-D shots #140076, 140083, 140093, 140094 and 140109.

model. The plasma response used to close the feedback loops was therefore idealized and assumed to be simply linear and governed by a full-order state-space model which, in the limit $\varepsilon \rightarrow 0$, reproduces the identified two-time-scale reduced-order

models. Note, however, that given the identified A_S , B_S , C_S , D_S and A_F , B_F matrices there is an infinite arbitrariness in the choice of a full-order model, as displayed in equations (4a) and (4b). In particular, the off-diagonal blocks of the full-order

model, A_{12} and A_{21} , contribute to the definition of A_S , and B_S , together with the diagonal blocks A_{11} and A_{22} [9], but A_{12} cannot be retrieved unequivocally from A_S and B_S .

The closed-loop response of the controller clearly exhibits the two-time scale convergence of the system towards the requested target, consistent with the characteristic time constants of the reduced-order slow and fast models which were 3.28 s and 0.38 s, respectively. In these simple linear simulations, the steady-state gains of the *closed-loop system*⁸ can be computed since the plasma response to the controller is given by a known model. The straight dotted lines in figure 8(a) show the final values that should be reached by each actuator, as anticipated from these closed-loop steady-state gains. The corresponding values of the controlled parameters are also shown by straight dotted lines in figure 8(b).

4. System identification experiments on DIII-D

The development of model-based profile control on DIII-D is motivated by the potential gain that it could yield in running stable and reproducible AT discharges, for studying the physics of integrated high-beta, high bootstrap current, steady-state scenarios for ITER. A set of dedicated experiments has therefore been performed in order to identify plasma models to be used in future control experiments. Using the same methodology as on JET and JT-60U, successful modelling of the DIII-D experiments will further assess the generic character of the semi-empirical ARTAEMIS approach for control-oriented plasma modelling on tokamaks, and the potential of the corresponding two-time-scale controllers.

For the DIII-D system identification experiments presented here, the chosen reference plasma state was that of a 1.8 T, β_N -controlled AT scenario, at a central plasma density, $n_{e0} \approx 3.5 \times 10^{19} \text{ m}^{-3}$ and plasma current, $I_p = 0.9 \text{ MA}$. The scenario had been developed to combine non-inductive current fractions near unity with normalized pressure $3.5 < \beta_N < 3.9$, bootstrap current fractions larger than 65%, and a normalized confinement factor, $H_{98(y,2)} \approx 1.5$ [12]. The NBI and ECCD systems provided the H&CD sources for these experiments. Available beamlines and gyrotrons were grouped to form, together with V_{ext} (equations (1a) and (1b)), five independent H&CD actuators: (i) co-current NBI power, P_{CO} , (ii) counter-current NBI power, P_{CNT} , (iii) balanced NBI power, P_{BAL} , (iv) total ECCD power from all gyrotrons in a fixed off-axis current drive configuration, P_{EC} , and (v) V_{ext} .

Actuator modulations were applied from $t = 2.5 \text{ s}$, i.e. after 1 s of a 0.9 MA current flat top. At this time, in all discharges, the V_{ext} control mode (i.e. the use of V_{ext} as an actuator) was enabled and the I_p and β_N controls were disabled. This is important as it ensures that there is no feedback in the response data when identifying the plasma response model. In addition to being a natural input variable in the model (equations (1a), (4a) and (5)), using V_{ext} as an actuator to control the current profile of the plasma during its transient evolution to an advanced non-inductive state is also a natural mode of operation in steady-state tokamaks: when sufficiently close to the required plasma state, controlled steady-state

⁸ The steady-state gain matrix of the closed-loop system relates the target values of the controlled parameters to the values they reach in steady state upon feedback action of the controller during closed-loop operation.

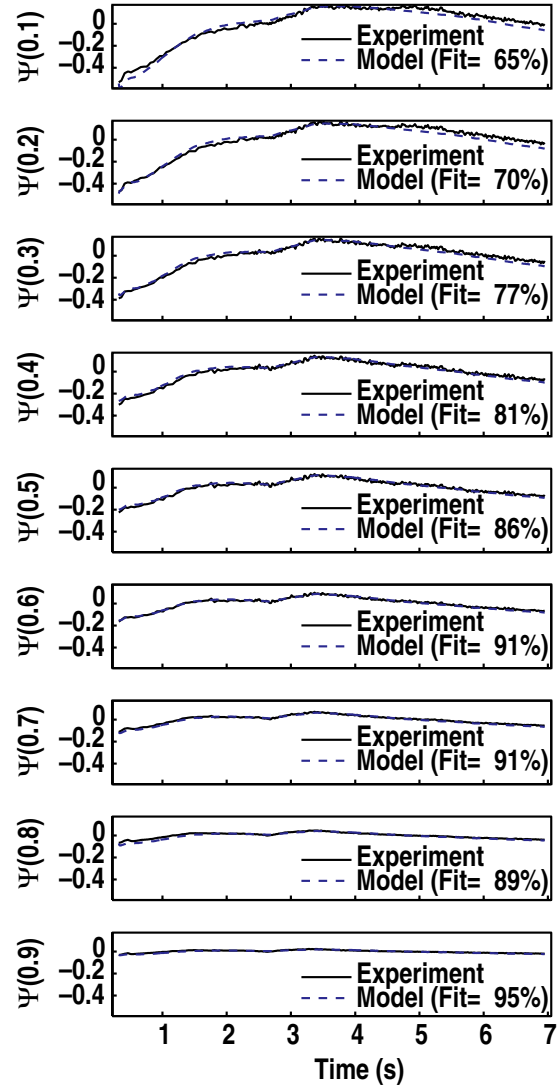


Figure 10. Comparison between the measured (black, full) and model-simulated (blue, dotted) Ψ data (Wb) at $x = 0.1, 0.2, \dots, 0.9$ for DIII-D shot #140093. The corresponding input data are shown in figure 9(a). The data for $t > 2.6 \text{ s}$ were used for system identification. Global fit: $f = 81\%$.

operation can be readily obtained by letting the weight of V_{ext} vanish with respect to other actuators in the near-optimal controller gain matrices. Altogether, 23 discharges were obtained, with I_p modulations in the range 0.7–1.2 MA, thus providing a broad database around the reference scenario. The undesired but measured variations of two additional parameters were included in the system as additional inputs that could be treated as disturbances and compensated for in future closed-loop operation. These were the gas injection rate, P_{GAS} , that was used in a density control loop, and the power, P_{CER} , from a beamline that was used for diagnostic purposes. Figures 9(a) and (b) display typical modulations of the system inputs and of the resulting plasma current, line-averaged density and normalized pressure.

System identification for the internal poloidal flux, $\Psi(x, t)$, was carried out with nine Galerkin coefficients computed at knots $x = 0.1, 0.2, \dots, 0.9$, starting at $t = 2.6 \text{ s}$.

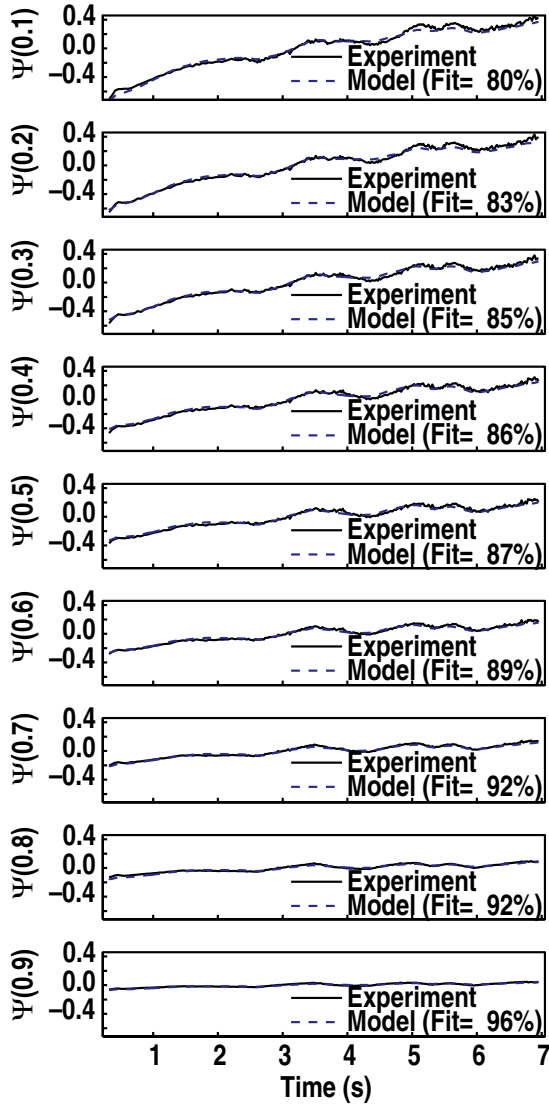


Figure 11. Comparison between the measured (black, full) and model-simulated (blue, dotted) Ψ data (Wb) at $x = 0.1, 0.2, \dots, 0.9$ for DIII-D shot #140094. The corresponding input data are shown in figure 9(a). The data for $t > 2.6$ s were used for system identification. Global fit: $f = 87\%$.

The search was initiated by a first guess of the static gain matrix simply obtained through Fourier analysis. Then, iterations were performed following the same technique as in section 3, i.e. gradually including more inputs and more discharges while fixing some columns of the static gain matrix corresponding to other inputs, and/or fixing some of the identified eigenvectors and eigenvalues when they were found to be physically sound and provide a good fit to the data. The dimension of the subspace and the static gain matrix used for the definition of the subspace was also updated when necessary while the iterations were executed. During all this process, the unfiltered input and output data could be used and the best model that was found was a model of order 5 in a subspace of dimension 5. The characteristic times corresponding to the eigenvalues of the A_S matrix were 5.46 s, 3.06 s, 1.98 s, 1.10 s and 0.023 s.

Figures 10–12 illustrate the typical fits of the experimental poloidal flux obtained from the model. As before an offset has been subtracted from all the datasets so that the measured data

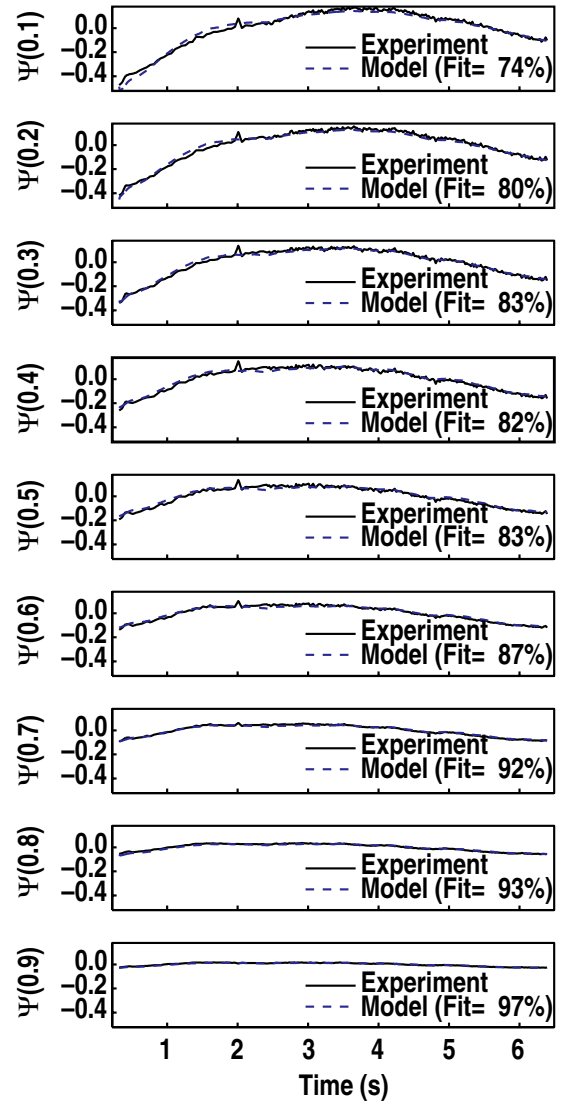


Figure 12. Comparison between the measured (black, full) and model-simulated (blue, dotted) Ψ data (Wb) at $x = 0.1, 0.2, \dots, 0.9$ for DIII-D shot #140075 (an $n = 1$ NTM is present from 2.3 s to the end). This shot was not used for system identification. Global fit: $f = 85\%$.

have zero average. It must be stressed that excellent fits are obtained for all shots, including shots that were not used in the identification process (see figure 12, for example). Moreover, for all discharges, the model fits the data satisfactorily starting from $t = 0.32$ s, i.e. not only during the phase when the identification was carried out but also during the current ramp-up phase. This is remarkable since only the data from $t = 2.6$ s, i.e. after 1 s of current flat top (see figure 9(b)), were used for model identification. Finally, another feature of interest of this magnetic model is that it also produces satisfactory $\Psi(x, t)$ fits for eight discharges that were affected by an unstable $n = 1$ neo-classical tearing mode (NTM), and for which the unstable phases were all disregarded for system identification. A typical example can be seen for shot #140075 (figure 12) where the $n = 1$ NTM appeared at $t = 2.35$ s and remained, with varying amplitude, during the whole duration of the high-power modulation phase ($2.5 \leq t \leq 7$ s). This means

Table 1. Model validation on shots performed prior to the system identification experiment.

Shot #	136206	136212	137537	137539	137559	137573	137575	137576
Flat-top current (MA)	1.4	0.96	0.96	1.4	0.96	1.15	1.4	1.15
Ramp-up time (s)	2.6 s	1.6 s	1.6 s	3 s	1.6 s	2.3 s	3 s	2.1 s
q_0/q_{\min}	3.5/2.2	1.6/1.6	2/2	2/2	3.4/3	1.6/1.5	2.3/1.8	2.2/2
Global fit	80%	65%	43%	91%	77%	87%	92%	90%

that the controller based on this relatively robust model (i) could be used to tailor the q -profile during current ramp-up and provide a favourable target for the high-power phase, and (ii) could also allow the discharge to recover from an unstable NTM due to a transiently unfavourable current density profile during the high-power phase.

An additional validation test was performed on a set of discharges which were obtained on DIII-D several months prior to the system identification experiment described here. In these discharges, different NBI and ECCD power waveforms were used during plasma current ramp-up in the aim of scanning the q -profile obtained at the end of ramp-up to study the effect of the current profile on plasma transport during the subsequent high-power, high-beta phase of AT discharges (current flat top). The toroidal magnetic field was 2 T, the flat-top plasma current varied between 0.9 and 1.4 MA and was obtained with various ramp-up rates. Both monotonic and non-monotonic safety factor profiles were obtained with central values, q_0 , ranging from 1.6 (monotonic) to 3.5 (non-monotonic), and with minimum values, q_{\min} , ranging from 1.6 (monotonic) to 3 (non-monotonic), at the beginning of current flat top. Model-predicted poloidal flux was compared with experimental data in these earlier discharges, during the ramp-up phases, in order to assess the possibility of controlling the current density profile in real-time during plasma ramp-up. For all these discharges, the measured and model-simulated data were very similar and the comparison was satisfactory, as it was for the identification discharges (see figures 10–12). The main characteristics of these validation discharges and the global fit parameters obtained in the validation tests are summarized in table 1.

Then, given the matrices A_S and B_S , a two-time-scale model for the coupled evolution of $\Psi(x, t)$ and $V_\Phi(x, t)$ was sought. Eight Galerkin coefficients computed at knots $x = 0.1, 0.2, \dots, 0.8$ were used for the V_Φ profiles, and only the data for $t \geq 2.6$ s were processed. The lowest frequency at which the inputs could be filtered while retaining a good fit of the unfiltered $\Psi(x, t)$ data by the slow model was found to be around 1 Hz. A cutoff frequency of 1 Hz was therefore chosen for separating the slow and fast components of both the input data and the toroidal rotation data in equations (5) and (6). The order of the final fast model for $V_\Phi(x, t)$ was 5, i.e. the same as the dimension of the subspace in which the model was sought, and characteristic times of 0.163, 0.128, 0.076, 0.058 and 0.038 s were obtained from the eigenvalues of the A_F matrix.

In a final step, the matrices, C_S and D_S , that represent the slow coupling between the poloidal flux and the toroidal rotation were identified. For this, as in section 3, the $V_{\Phi,F}$ data predicted by the fast model using the fast inputs, P_F (see equation (6)), were removed from the measurements. Since the fast model is not perfect, the resulting signals still contained

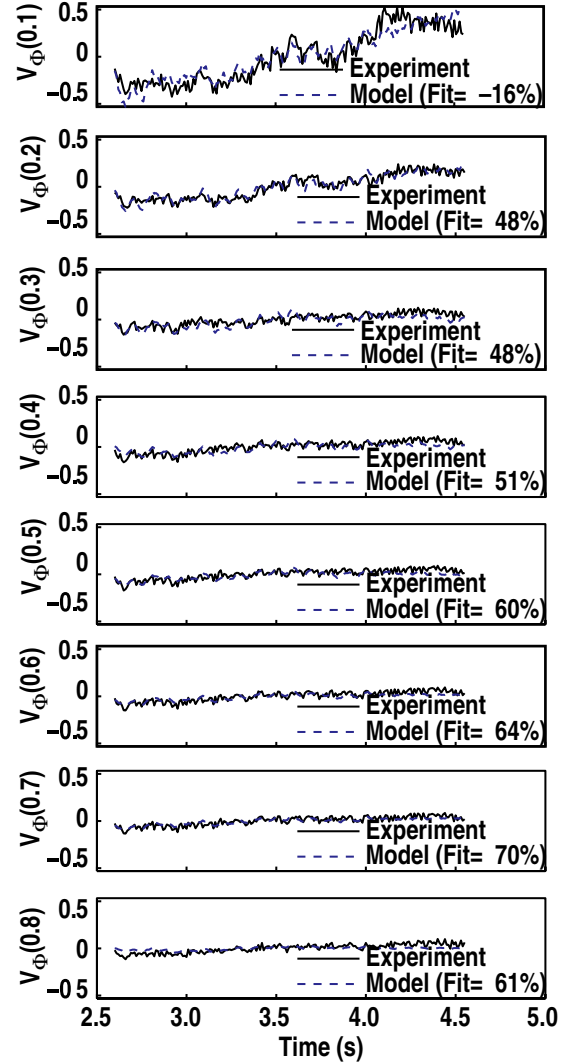


Figure 13. Comparison between the measured (black, full) and model-simulated (blue, dotted) V_Φ data at $x = 0.1, 0.2, \dots, 0.8$ for DIII-D shot #140074. Global fit: $f = 51\%$.

frequency components above 1 Hz. They were also filtered out to retain only slowly evolving data. Altogether, when combining the slow and the fast models with the coupling equations (5) that contain the identified C_S and D_S matrices, the resulting two-time-scale model for the coupled evolution of $\Psi(x, t)$ and $V_\Phi(x, t)$ was a model of order 10, with a resistive diffusion time of 5.4 s and a momentum confinement time of 0.16 s. Figures 13–15 illustrate typical fits obtained for $V_\Phi(x, t)$ with the full model.

The essential elements of the identified state-space response model are the steady-state (or static) gain matrix of the system, $K_S = -(C_S \cdot A_S^{-1} \cdot B_S) + D_S$, and the eigenmodes of A_S

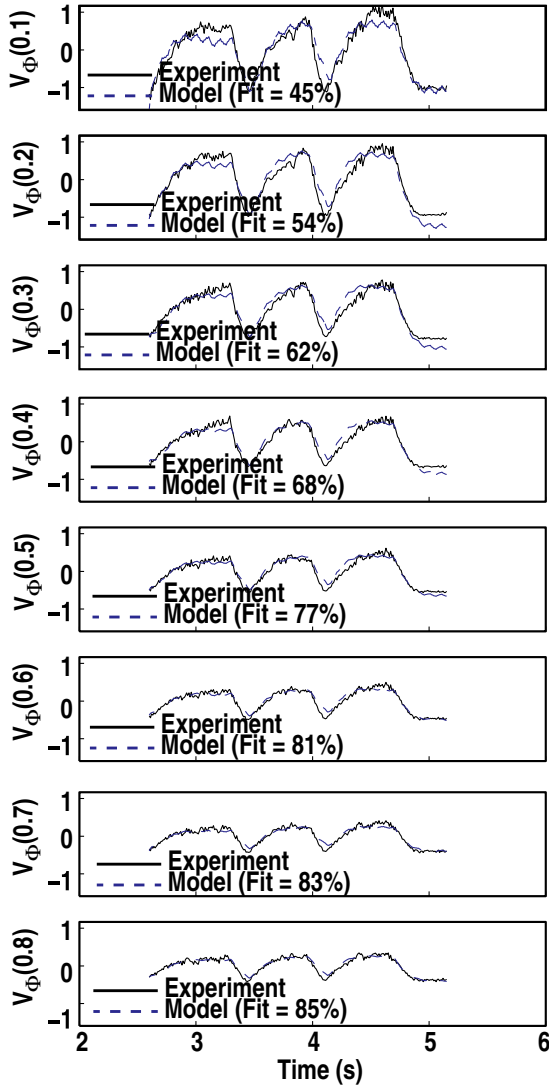


Figure 14. Comparison between the measured (black, full) and model-simulated (blue, dotted) V_ϕ data at $x = 0.1, 0.2, \dots, 0.8$ for DIII-D shot #140076. Global fit: $f = 68\%$.

and A_F with their corresponding eigenvalues or characteristic times. A representation of the static gain matrix of the identified tenth order model can be seen in figure 16 where the steady-state response of the poloidal flux and plasma rotation profiles to unit change of the various inputs in the model are plotted.

A number of remarks can be made about this diagram in which powers are expressed in MW, loop voltage in units of 0.1 V and gas flow in units of 10 Torr l s^{-1} . Unsurprisingly, the most powerful actuator for changing the current profile in absolute terms is indeed the loop voltage, in other words the ohmic transformer, as voltages of 0.5 to 2–3 V are routinely obtained during plasma current ramp-up. In contrast, the total power capability of the three beamlines that constitute the co-current NBI actuator is of the order of 7.5 MW (as seen, for example, in figure 9(a)). In addition, one of these beamlines cannot really be used as a control actuator because it is precisely needed for measuring, through the MSE diagnostic (motional Stark effect), the plasma poloidal flux profile to be controlled.

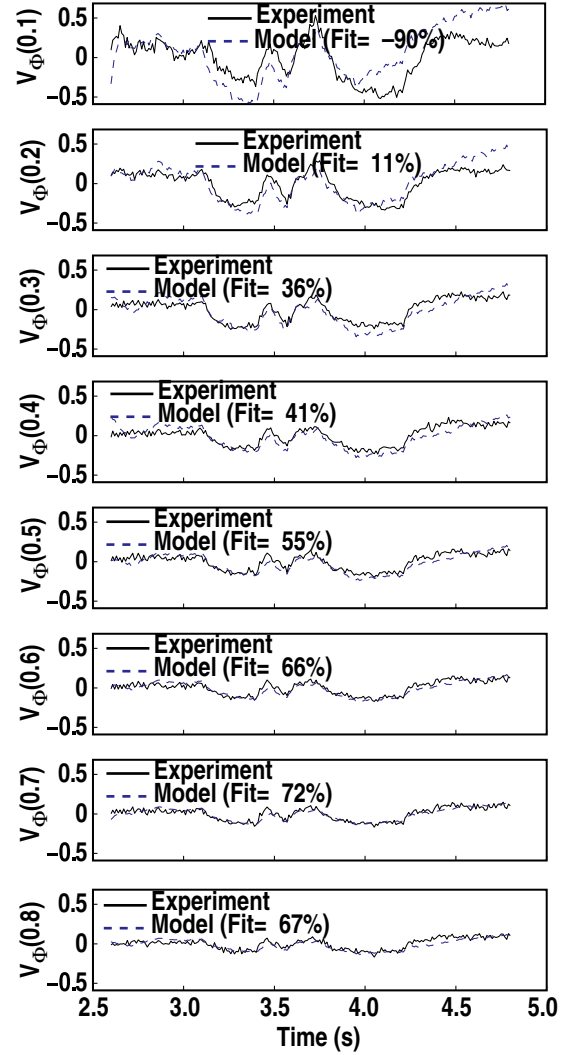


Figure 15. Comparison between the measured (black, full) and model-simulated (blue, dotted) V_ϕ data at $x = 0.1, 0.2, \dots, 0.8$ for DIII-D shot #140106. Global fit: $f = 30\%$.

Nevertheless, co-current NBI is the second most powerful actuator for changing the poloidal flux profile, and therefore the current profile.

The response of the poloidal flux profile to the co-current and counter-current NBI actuators is found to be very asymmetrical and, consistently, balanced injection leads to an increase in the poloidal flux or plasma current. However, the uncertainties in these responses are difficult to evaluate. For the poloidal flux, rough estimates could be obtained from the standard deviations of the various columns of the B_S matrix during the final iterations of the identification process where the A_S matrix was fixed. They are plotted in figure 16. The standard deviation of the A_S matrix elements when the steady-state gains are fixed has also been estimated and corresponds to a relative variation of 4% for the norm of A_S . The asymmetry between co- and counter-current NBI is in qualitative agreement with detailed experimental investigations on beam-ion confinement for different injection geometries [13]. These studies showed that tangential counter-current injection results in a lower fast-ion confinement in

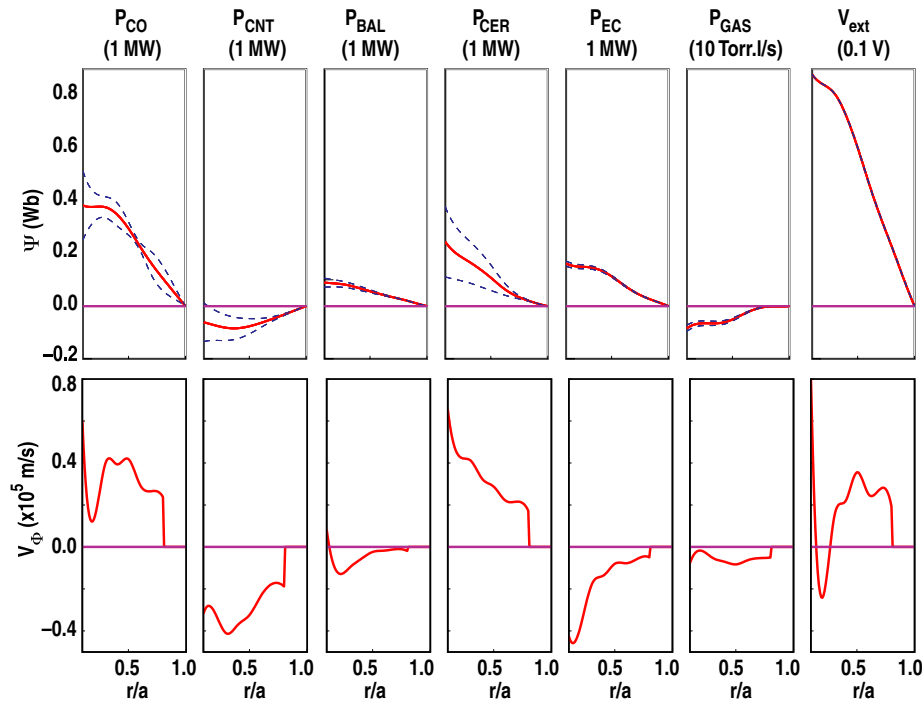


Figure 16. Representation of the model steady-state gain matrix. Each column represents the variation of the poloidal flux (top) and toroidal rotation (bottom) profiles corresponding to unit positive step variation of a given input. Columns #1–7 correspond to P_{CO} (MW), P_{CNT} (MW), P_{BAL} (MW), P_{CER} (MW), P_{EC} (MW), P_{GAS} (10 Torr.l s⁻¹) and V_{ext} (0.1 V), respectively. Estimates of the uncertainties for the poloidal flux response are shown in the top frames (dotted).

comparison with co-current injection, and that the counter-injected beams disappear faster through thermalization or charge exchange losses. This necessarily leads to a reduction in current drive efficiency. The difference between the experimental observations and the results of simulations based on classical fast-ion transport was also found to be larger than the estimated uncertainties [13]. Counter-current NBI is therefore not expected to be a powerful actuator for current profile control only, but it can be essential in providing some decoupling between current drive and rotation drive in magneto-kinetic control. Balanced injection could have a more specific role in decoupling the current and rotation control from, say, the ion temperature or pressure control but this will be the subject of future investigations.

The last point worth mentioning is the non-local effect of the off-axis ECCD actuator on the toroidal plasma rotation in the centre of the plasma. Such rotation braking in the plasma core has indeed already been observed on DIII-D [14] and on other tokamaks [15, 16]. The fact that this effect can be detected by the present system identification algorithms is indeed worth noticing.

5. Conclusion

In order to extend advanced tokamak scenarios to steady-state operation, the plasma state, as defined by a number of parameter profiles such as the poloidal flux, current density, plasma density, velocity and temperature, will have to be controlled in real-time. For this purpose, the experimental system identification and control methodology that was initially developed for JET profile control experiments has now

been generalized for magneto-fluid control on other devices, with different sets of actuators and sensors. In this work, the resulting *ARTAEMIS* algorithms and computer routines have been applied to the identification of dynamical models for the coupled evolution of various magnetic and fluid/kinetic parameter profiles on JT-60U and DIII-D.

The system has the structure of a state-space model in which some physical variables appear naturally as the state, output and input variables, respectively. Singular perturbation methods are used to take advantage of the small ratio between the confinement and resistive diffusion time scales (two-time-scale approximation). This method was shown to yield *control-oriented*, reduced-order models which could fairly reproduce the slow and the fast evolution of coupled plasma parameter profiles, in a broad vicinity of a reference equilibrium plasma state which need not be known explicitly. In this study, the controlled plasma variables were chosen to be the inverse safety factor or the poloidal flux, the toroidal rotation velocity and the ion temperature. The actuators are the H&CD powers, and the plasma surface loop voltage can be used as an additional actuator if it is adequately controlled by the poloidal field system. A linear closed-loop simulation using the two-time-scale model derived from the JT-60U data was shown in order to illustrate, on a simple example, how magnetic *and* fluid/kinetic parameter profiles could be simultaneously controlled using the proposed strategy and algorithms.

This semi-empirical method provides, for control purposes, a *readily available* alternative to first-principle plasma modelling. It was shown that it can be used in different devices, for simple as well as more comprehensive controls, with different sets of actuators and sensors, and that

the identified models describe satisfactorily the dynamics that are considered relevant for magneto-kinetic plasma control. New experimental investigations on pulsed (DIII-D, ASDEX Upgrade) and steady-state tokamaks (Tore-Supra, EAST, KSTAR, SST-1 and later JT-60SA) would also be beneficial to fully assess the accuracy and robustness of the identified response models, and of the controllers based on them, in order to achieve magneto-fluid plasma state control in steady-state scenarios. The experimental identification of such *control-oriented* models will open the way to the development of real-time profile control as an essential means of achieving advanced tokamak operation in steady state—a requirement for a steady-state fusion reactor—and may provide a lead for developing advanced kinetic control in ITER.

Acknowledgments

This work, supported by the European Communities under the contract of Association between EURATOM and CEA, was carried out within the framework of the European Fusion Development Agreement and in part by the US Department of Energy under DE-FC02-04ER54698 and DE-FG02-92ER54141. The views and opinions expressed herein do not necessarily reflect those of the European Commission. The first author is very grateful to the Takase-Ejiri Laboratory (University of Tokyo), the JT-60U Team and the DIII-D Team, for their help and hospitality, and also to the International Tokamak Physics Activity (ITPA) Coordinating Committee and

Integrated Operation Scenarios topical group for supporting this Joint Research.

References

- [1] Romanelli F. and Kamendje R. on behalf of JET-EFDA Contributors 2009 *Nucl. Fusion* **49** 104006
- [2] Oyama N. and the JT-60 Team 2009 *Nucl. Fusion* **49** 104007
- [3] Strait E.J., for the DIII-D Team 2009 *Nucl. Fusion* **49** 104008
- [4] Gormezano C. *et al* 2007 Progress in the ITER Physics Basis Chapter 6: Steady state operation *Nucl. Fusion* **47** S285
- [5] Gribov Y. *et al* 2007 Progress in the ITER Physics Basis Chapter 8: Plasma operation and control *Nucl. Fusion* **47** S385
- [6] Ljung L. 1999 *System Identification: Theory for the User* (Upper Saddle River, NJ: Prentice Hall PTR)
- [7] Moreau D. *et al* 2003 *Nucl. Fusion* **43** 870
- [8] Laborde L. *et al* 2005 *Plasma Phys. Control. Fusion* **47** 155
- [9] Moreau D. *et al* 2008 *Nucl. Fusion* **48** 106001
- [10] Kokotovitch P.V., Khalil H.K. and O'reilly J. 1986 *Singular Perturbation Methods in Control: Analysis and Design* (London: Academic)
- [11] Sakamoto Y. *et al* 2009 *Nucl. Fusion* **49** 095017
- [12] Holcomb C.T. *et al* 2009 *Phys. Plasmas* **16** 056116
- [13] Heidbrink W.W. *et al* 2009 *Plasma Phys. Control. Fusion* **51** 125001
- [14] de Grassie J.S. *et al* 2007 *Phys. Plasmas* **14** 056115
- [15] Yoshida M. *et al* 2009 *Phys. Rev. Lett.* **103** 065003
- [16] Mcdermott R.M. *et al* 2010 *Proc. 37th EPS Conf. on Plasma Physics (Dublin, Ireland 21–25 June)* P1.1062 <http://ocs.ciemat.es/EPS2010PAP/pdf/P1.1062.pdf>